



Effects of solution ageing in compressive behaviour of SLM-In718 triply periodic minimal surfaces

Mobin Majeed¹ · Rong Situ¹ · Zia Javanbakht^{2,3}

Received: 8 July 2024 / Accepted: 8 February 2025
© The Author(s) 2025

Abstract

This study aims to investigate the effect of heat treatment on the microstructure and mechanical properties of triply periodic minimal surface (TPMS) structures manufactured by selective laser melting (SLM) from Inconel[®] alloy 718 (In718). Although many aspects of SLM-In718 have been studied, its as-built (AB) and heat treated (HT) performance under compression has not been thoroughly investigated. To this end, sheet-based diamond, gyroid, and primitive morphologies along with bulk specimens were manufactured and tested under AB and HT conditions. Standard solution ageing (solution treatment + two-step ageing) was carried out to improve some of the inherent deficiencies of SLM-In718 such as the development of brittle Laves and δ phases. It was found that the overall mechanical performance of the HT TPMS specimens were improved in terms of stiffness, strength, and energy absorption among others. Furthermore, the geometry of the TPMS specimens dictated the extent of enhancement such that the diamond geometry outperformed the others in many aspects. In contrast, the primitive structure demonstrated the most stable plateau stage in both AB and HT conditions. Microstructural analysis revealed occasional precipitation of second-phases carbide particles at grain boundaries. Moreover, niobium was made available by dissolution of Laves phases during solution treatment which was later used in precipitation of strengthening γ' and γ'' phases during ageing. Finally, a new scheme for analysing the energy absorption was devised which could provide a new perspective towards studying energy efficiency of porous structures. Accordingly, it was found that heat treatment improves the mechanical properties contributing the first two stages of energy absorption (initial and plateau) while limiting the fraction of the final stage. In conclusion, it was demonstrated that although heat treatment could address issues like residual stresses and microstructural shortcomings of SLM-In718, the extent of this rectification is further controlled by cell topology of the TPMS structure.

Keywords Selective laser melting · Ageing · Solution treatment · Solution ageing · Nickel-based superalloy

1 Introduction

TPMS structures Lattices are architected cellular materials which are endowed with periodic voids because of their strut-, skeletal-, or sheet-based design [1]. The structure of the first category is comprised of struts whereas the latter two are formed by minimal surfaces. A surface is *minimal* when the average of principal curvatures spatially vanishes [2]. A triply periodic minimal surface (TPMS) structure is a periodic lattice that can be developed using either skeletal- or sheet-based unit cells along three perpendicular directions. Examples of similar periodic structures exist naturally which could imply their evolutionary enhancement through time, e.g., butterfly wings [2], trabecular bone [3], sea urchin skeletons, and wood [4]. Advantages of TPMS structures

✉ Zia Javanbakht
z.javanbakht@griffith.edu.au
Mobin Majeed
mobin.majeed@my.jcu.edu.au
Rong Situ
rong.situ@jcu.edu.au

¹ College of Science and Engineering, James Cook University, 1 James Cook Dr, Townsville, QLD 4814, Australia

² School of Engineering and Built Environment, Griffith University, 1 Parklands Dr, Gold Coast, QLD 4215, Australia

³ AuxeticsLab, Advanced Design Prototyping Technologies Institute (ADaPT), Griffith University, 1 Parklands Dr, Gold Coast, QLD 4215, Australia

have been reported in terms of superior specific properties (e.g., strength and energy absorption), biocompatibility (e.g., osseointegration and tissue generation), and conductivity (e.g., heat and electricity) among others [1, 4–6]. Furthermore, their mechanical properties can be versatily adjusted through various design parameters for a given application.

Mechanical characteristics of TPMS structures Design (cell topology), relative density, and base material properties can control some of the mechanical characteristics of TPMS structures [7, 8]. Overall, sheet-, strut-, skeletal-based design provide best mechanical properties in descending order [9] although there are exceptions. Under each category, the selection of topology highly impacts the mechanical response. For instance, diamond structure displays excellent stress–strain response, followed by gyroid and primitive topologies [10]. Although the effects of relative density cannot be conclusively predicted, increasing relative density improves mechanical properties (e.g., compressive strength, stiffness, yield strength, plateau stress, stress distribution, and EA) [10]. The dominating effects of topology at low relative densities is diminished at higher levels where asymptotically moves towards those of the base/bulk material. On the other hand, exceptionally low relative densities may suffer from stress concentration which drastically changes the deformation mode of the structure [11]. Contra-intuitively, a diamond sheet-based TPMS structure was reported to have mechanical properties almost independent of its density [9]. While acknowledging the extreme or exceptional cases, a better understanding is anticipated by investigating the common deformation mechanisms of these structures.

Deformation modes of TPMS structures Identifying a concrete trend to predict the deformation mode of lattices is a complicated process because of the numerous factors involved. Primarily, mechanical characteristics of TPMS structures dictate their deformation mode, i.e., bending, stretching, and twisting of the internal elements [12], which can also show layerwise alternation in a single structure [13]. For a specific cellular structure, the deformation mechanism depends on the loading type, e.g., a bending dominated behaviour can shift to stretch domination by changing the type of loading [12]. Given the same relative density, bending-dominated lattices underperform stretching-dominated ones in strength and stiffness—while under compression, stretch-dominated mechanisms suffer from post-yield softening [14]. In contrast, sheet-based TPMS structures are stretch dominated under compression and outperform skeletal-type TPMS structures with a bending-dominated behaviour (at similar relative density) [9]. Further to the aforementioned points, an additional complexity is introduced by additive manufacturing (AM), i.e., the inherent

requirement of post processing to improve the as-built (AB) condition of the base material.

Post-processing of TPMS structures Stress concentration [11, 15], eigenstresses [16], and imperfections [17] have undesired prevalent effects in thin-walled structures created by AM. For Skeletal-based TPMS structures, compression-compression fatigue [18], energy absorption [19], and failure mode [20] can be improved by heat treatment. In addition, residual stresses can be removed through additional stress relieving cycle [21, 22]. Although that deformation mode predictions might not be quite scalable towards low densities, heterogeneous mass distribution along with thin connections aggravate the situation [11]. General approach for improving energy absorption is controlling the post-yield response, i.e., by retaining a stable plateau stage [19, 23, 24] and avoid any strain softening [18, 25]. Taking advantage of the macroscopic properties of TPMS structures requires a careful attention to the microstructure of the base material.

Application of TPMS structures and base material TPMS structures are extensively used for energy absorption (EA), crashworthiness, and impact loading [26, 27] where a particular field of application is dictated by the used base material and manufacturing capabilities. For instance, aerospace and automotive industries started using high-strength AlSi10Mg [28] for complex geometries after the introduction of selective laser melting (SLM) while the wrought or cast of the same alloy were/are unattractive options [29]. TPMS biomedical implants are made of Ti6Al4V [30], CoCr [31], or 316 L [32] for their biocompatibility. Particularly to our interest is the Inconel[®] superalloy 718 (In718) which provides excellent mechanical properties at elevated temperatures along with high corrosion resistance [33] and good weldability [34]; nevertheless, it suffers from a high density ($\rho_s = 8.19 \text{ g/cm}^3$) [35]. The latter aspect can be compensated by combining the excellent base material properties with the features of TPMS structures. This approach has created opportunities for SLM-In718 in high performance application such as jet engine parts [36] and turbine blades [37]. For instance, optimised In718 TPMS turbine blades have shown improved specific properties compared to those built from the bulk base material (40.32% mass reduction and stress reduction of 48.55%) [37]. Nevertheless, obtaining a high material performance through SLM demands post processing for most nickel-based alloys [38].

Microstructure of additively manufactured AB In718 The mechanical properties of AB SLM-In718 falls behind those created by conventional manufacturing [38]. In Ni-based γ austenite matrix of In718, γ' Ni₃(Al,Ti,Nb) and γ'' Ni₃(Nb,Ti) are major precipitation strengthening phases along with strengthening carbides/nitrides MX (Nb,Ti)(C,N) [39, 40].

In contrast, undesirable brittle Laves $(\text{Ni,Fe,Cr})_2(\text{Nb,Mo,Ti})$ and δ phases (Ni_3Nb) are created by microsegregation of Nb and Ti, which deprives the strengthening phases of their major required components [39, 41]. It should be noted that certain levels of δ and carbide phases can be effective in grain boundary pinning [22, 41]. Inherent characteristics of SLM (e.g., thermal gradient along build direction, melt pool size, and partial remelting of previous layers) [42, 43] create some impairing microstructural effects in AB In718 such as:

- increased porosity [39] or void content/size [22],
- cellular (in cross-section) and columnar (longitudinal, along laser movement [44]) γ phase [40] with dendritic morphology [43];
- macroscopic molten pool boundaries forming fish-scale patterns that consists of very fine columnar dendrites [43, 45],
- scarcity of strengthening phases [38], and
- interdendritic Laves phases [43].

To improve the microstructure of AB SLM-In718, such shortcomings should be addressed by heat treatment.

Post-processing of AB SLM-In718 specimens Heat treatment of SLM-In718 is mainly based on the procedures developed for conventional manufacturing methods [21, 22] but designing an efficient procedure depends on many factors such as the laser deposition method, solidification, and thermal effects among others [38]. However, a combination of following steps is commonly used in post processing of AB SLM-In718:

- Hot isostate pressing* is used to reduce the void size and porosity, often for cast and wrought In718 [22, 46].
- Stress relieving* is applied (prior to removal from built plate) to remove residual stresses [22].
- Homogenisation treatment* (H) minimises elemental segregation [22], removes columnar cells and the laser path trace [44], releases Nb from Laves phase, and homogenises the elemental distribution [47].
- Solution treatment* (ST) recrystallises columnar grains to equiaxed ones [22, 41], recrystallises the dendritic microstructure [41], dissolves interdendritic Laves phases, and releases Nb into the matrix [46].
- Direct ageing* (DA) precipitates γ' and γ'' phases using the available Nb [45].

Overall, for precipitation of strengthening phases, DA is sufficient but it cannot resolve the columnar structure and dissolve Laves phases [38]. In this sense, H and/or ST should be used to remove the Laves phases and make

the required Nb available for precipitation during DA. Thus, their sequential use is more effective, i.e., using the ST+DA procedure which is called *solution ageing* (SA). It is worth mentioning that with optimised SLM parameters, using a separate homogenisation step seems trivial [22]. However, a H+ST+DA procedure precipitates carbide and δ phases into grain boundaries and promotes the pinning effect [38, 47]. Additional parameters of heat treatment are temperature and dwell time of each procedure in addition to the cooling rate, i.e., quenched, slow cooled, and furnace cooled [22, 41, 47]. A heat treatment can be any combination of the above procedures, e.g., ST+DA2 which consists of solution treatment and two-step ageing. It seems that a comprehensive investigation should cover the microstructural aspects of SLM-In718 as base material (in AB and post processed conditions) along with the macroscopic characteristics of the TPMS structure.

Motivation and aim Most of the current heat treatment research focus on the bulk specimens [38] and thus, ignore the solidification conditions and thermal gradients of complex geometries such as TPMS structures; inferior mechanical properties of AB TPMS structures asserts this point. Heat treatment has improved the microstructure and mechanical properties of TPMS structures fabricated from 316 L [48], Ti6Al4V [49], and AlSi10Mg [20]. Therefore, it is hypothesised that heat treatment can also improve the mechanical properties of AB In718 TPMS structures in a similar fashion. Herein, it is aimed to investigate the effects of SA on three sheet-based TPMS topologies (diamond, gyroid, and primitive) manufactured from In718. Considering the AB and HT conditions, the objectives are:

- to investigate the microstructural changes of bulk specimens, and
- to characterise the change in the mechanical performance and surface quality of the TPMS specimens, and
- to challenge the energy absorption efficiency metrics in this context.

To this end, microstructural features were characterised in scanning electron microscope (SEM) and standard compression tests were conducted to obtain the mechanical properties. After providing the details of these procedures in the methodology section, the results are presented and discussed. Particularly, energy absorption fractions were analysed within a new scheme. The study concludes with the main findings and provides the possibilities for future trajectory of the current research.

2 Methodology

2.1 Designing, manufacturing, and heat treatment

Designing the TPMS and bulk samples The topology of three high-performing TPMS structures is obtained from trigonometric functions: primitive $f_p(x, y, z)$, diamond $f_d(x, y, z)$, and gyroid $f_g(x, y, z)$ isosurfaces were designed using the following level set approximations [10]:

$$f_p(x, y, z) := \cos(\alpha x) + \cos(\alpha y) + \cos(\alpha z) = t/2, \quad (1a)$$

$$f_d(x, y, z) := \cos(\alpha x) \cos(\alpha y) \cos(\alpha z) - \sin(\alpha x) \sin(\alpha y) \sin(\alpha z) = t/2, \quad (1b)$$

$$f_g(x, y, z) := \sin(\alpha x) \cos(\alpha y) + \sin(\alpha y) \cos(\alpha z) + \sin(\alpha z) \cos(\alpha x) = t/2, \quad (1c)$$

where $\alpha := 2\pi/l$ controls the repeating period of the structure (cubic unit cell with a period of l along the three Cartesian coordinates x , y , and z); and $t/2$ is the iso-value that controls the volume fraction of each unit cell. The surface corresponding to $t = 0$ results in 50% solid volume fraction (i.e., relative density) and can be safely used as a mid-surface to create the required thickness (t) in normal inward and outward directions ($\pm t/2$). To this end, the zero level set surfaces were exported from MATLAB to nTopology commercial package for extrusion. Finally, TPMS structures with four cubic unit cell of edge length $l = 4$ mm along three perpendicular directions were created; the volume of $16 \times 16 \times 16 \text{ mm}^3$ has been reported to be a good representative of an infinitely periodic structure [50], see Fig. 1. Additionally, two bulk printed samples ($18 \times 18 \times 18 \text{ mm}^3$) were manufactured. Further details are provided in the sequel.

Manufacturing and heat treatment procedures The TPMS and bulk specimens were manufactured in an AM400 SLM machine (build size: $250 \times 250 \times 300 \text{ mm}^3$; Renishaw, UK) using gas atomised In718 powder under controlled argon atmosphere. The In718 powder was supplied by Renishaw in accordance with ASTM B637 [51] and melted under optimised manufacturing parameters. The samples were separated from the build plate by wire electric discharge machining and exhibited a good dimensional accuracy. Following this approach, eight samples per TPMS design were manufactured (24 samples in total) of which half kept in AB condition and the other half was heat treated (HT) according to AMS 2773 [52]. Similarly, one of the two bulk samples undergone heat treatment, see Table 1. Mechanical and microstructural characterisation of the samples was carried out afterwards. Note that for each condition, three out of

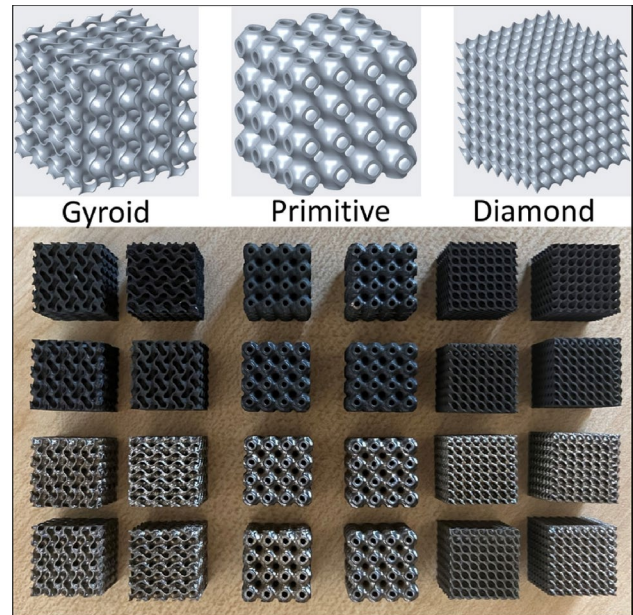


Fig. 1 Three designed sheet-based TPMS structures (HT specimens are darker in colour compared to the AB samples)

four samples per TPMS design was selected for statistical analysis.

2.2 Mechanical and microstructural characterisation

Surface preparation and characterisation of bulk printed In718 Surface preparation of bulk In718 specimens consisted of grinding with 200–2000 grit SiC papers, fine polishing with diamond suspension, and final polishing in a colloidal silica suspension. Then, the specimens were cleaned in an ultrasonic bath with ethanol medium, followed by water rinsing to remove any residues. Finally, the specimens were etched with a blend ($100 \text{ ml C}_2\text{H}_5\text{OH} + 100 \text{ ml HCl} + 5 \text{ g CuCl}_2$) for a few seconds. Microstructure of the prepared samples was analysed using a Hitachi SU5000 SEM equipped with Energy-dispersive X-ray spectroscopy (EDS) analysis system. The machine was operated at 20 kV and a working distance of $11.3 \mu\text{m}$ during the analysis.

Mechanical testing of TPMS structures Displacement-controlled compression testing of the TPMS samples (crosshead speed of 2 mm/s) was carried out on a 50 kN Shimadzu universal testing machine in accordance with ISO 13314: 2014 [53, 54]. Using the force-displacement data, average engineering stress (σ) was calculated as the ratio of the compressive force to the gross undeformed cross-sectional area of

Characterising the TPMS energy absorption Energy absorption (W) and specific energy absorption (W_s) are defined as functions of strain (ϵ):

$$W := \int_0^\epsilon \sigma \, d\epsilon, \quad (5a)$$

$$W_s := \frac{W}{m}, \quad (5b)$$

where σ is the engineering stress. A common energy absorption efficiency definition is [56]:

$$W_e := \frac{W}{\sigma}, \quad (6)$$

where ϵ is the total strain and σ is its corresponding stress. The second efficiency metric is ‘ideality’ [53, 56]:

$$W_i := \frac{W}{\sigma\epsilon}, \quad (7)$$

where ϵ is the total strain and σ is its corresponding stress. It is worth mentioning that ideality is called ‘energy absorption efficiency’ in [53]. Ideality gauges the energy absorption capacity of a foam against an ideal foam, see [56] for details.

3 Results and discussion

3.1 Microstructural characterisation of bulk AB In718 specimens

Grains in bulk In718 in AB state AB In718 has an anisotropic heterogeneous microstructure because of the columnar grains, columnar dendrites inclined along the build direction (z -axis), and the formation of fish scale shape melt-pool, see Fig. 2. AB In718 possesses columnar grains mainly aligned with the build direction resulting in anisotropic properties. Columnar grains were formed along the metal deposition (build direction) due to the cooling direction and repeated remelting of previously deposited layers. This repetition causes a strong bond between successive layers, formation of longer columnar grains, and reduces the risk of delamination. The formation of the fish scale shape along the build direction is ascribed to the Gaussian distribution of the laser heat source [54], see Fig. 2a. Microstructure of AB In718 consists of mainly cell and columnar crystals. Fine columnar dendrites tend to grow in multiple directions because of their tendency to form in the opposite direction of temperature gradient, see Fig. 2b. Temperature gradient is perpendicular to the melt-pool boundary—which is constantly changing, owing to the Gaussian nature of the laser heat source [57]. However, due to directional cooling in the SLM process,

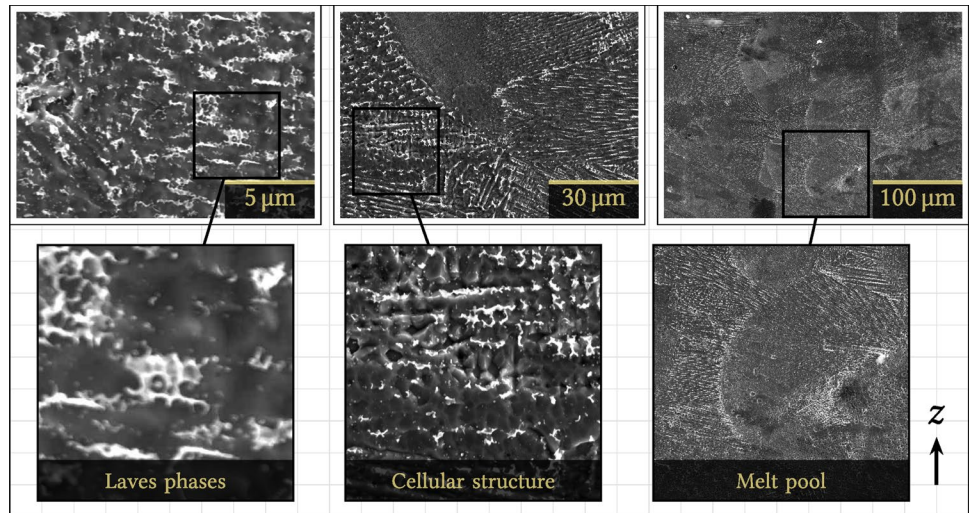
the dendrites are mainly aligned with the build direction and contribute to anisotropy [58]. Microsegregation of alloying elements in the inter dendritic region adds further non-homogeneity to this anisotropic micro-feature.

Microsegregation and phases in bulk AB In718 In bulk AB SLM-In718 specimens, rapid solidification results in the segregation of elements such as Nb and Mo in the interdendritic regions—which precipitates detrimental phases and restricts the precipitation of strengthening phases. Microsegregation of Nb and Mo alloying elements in the inter-dendritic regions develops a higher volume of detrimental phases such as δ , carbides, and Laves phase therein [59]. Higher consumption of Nb by these phases [57] suppresses the formation of primary strengthening phases (γ' and γ'') in the matrix [58]. In Fig. 2a, dark regions contain relatively high concentrations of Ni, Cr, and Fe (γ phase) whereas white regions consist of the inter-dendritic Laves phase (with additional Nb and Mo). EDS confirms these compositions which are consistent with the analysis presented in [36], see Fig. 3. The brittle Laves phase is susceptible to crack nucleation/growth [43] and thus, demotes the mechanical performance. Non-equilibrium microstructure, microsegregation, and suppression of strengthening phases in AB SLM-In718 cause inferior mechanical properties, demanding a post treatment.

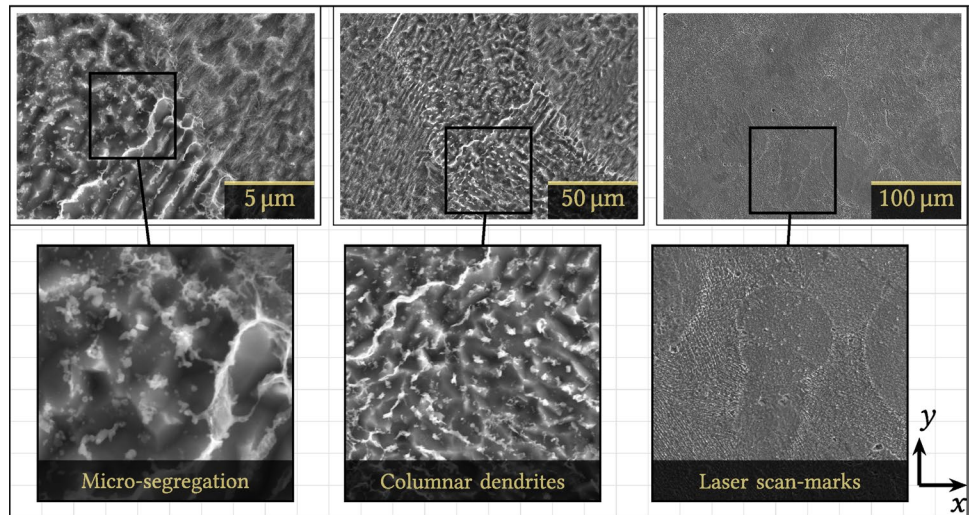
3.2 Microstructural characterisation of bulk SA In718 specimens

Transformation of microstructure along the build direction Along the build direction (z -axis), SA dissolved some Laves phases, precipitated the strengthening phases, and removed melt pool marks whereas acicular δ -phase at grain boundaries and columnar grains remained. During ST, dissolution and diffusion of elements such as Nb facilitates the precipitation of strengthening phases (γ' and γ'') in DA [60]. In AB condition, the complex melt pool dynamics and high cooling rate [28] in SLM process suppress the formation of γ' and γ'' strengthening phases. However, with sufficient holding temperature and dwell time in ST, Nb and Ti elements are diffused into the γ -matrix to form γ' -(Ni₃(Al,Ti)) and γ'' -(Ni₃Nb) phases during DA. These phases are identified through their distinctive morphology [58, 61], i.e., the needle-like γ'' -precipitates are evenly distributed inside the matrix and δ -phase at grain boundary, see Fig. 4. Moreover, the scan marks of melt pools were faded after SA. Although heat treatment at 980°C was not enough to dissolve Laves phases, it was sufficient for the development of acicular δ -phase [44] at grain boundaries and thus, inhibiting grain boundary sliding [62]. Additionally, because δ -phase consumes less Nb than the Laves phase, the extra Nb dissolves

Fig. 2 SEM characterisation of AB In718 microstructure along build direction and on the build plane: **a** white Laves phase, cellular structure of grains, and fish-scale pattern of the melt pool in the build direction (z -axis), and **b** mixed dendrites and laser scan-marks on the build plane (xy -plane). Note that darker regions represent the γ matrix



(a)



(b)

back into the matrix during ST [45] and further promotes the formation of strengthening precipitates during DA. After DA, most of the columnar grains persisted, which indicates that a full recrystallisation did not occur during ST; similar results were reported in [41]. On the build plane, a microstructure similar to that along the build direction existed.

Transformation of microstructure on the build plane Similar to the build direction, strengthening phases, acicular δ -phase at grain boundaries, and MC carbide particles were observed on the build plane (xy -plane); furthermore, disappearance of dendritic features and fish-scale patterns was accompanied by the development of equiaxed grains after heat treatment, cf. Figures 4b and 2b. The grain boundaries can also be identified by some δ -phase with acicular morphology and MC carbide blocks, see Fig. 4b. Presence of these two features provides additional strength to material by pinning the grain

boundaries and limiting grain growth. Heat treatment was sufficiently efficient in removing the dendritic microstructure and annihilating the fish-scale pattern on the surface. Isotropic dissipation of heat resulted in developing some equiaxed fine grains while most of the columnar structure still existed. Thus, anisotropy is slightly reduced while grain refinement is expected to work in favour of strength.

Post-SA carbide particles in bulk SLM-In718 samples Stable NbC carbide particles (with a composition rich in Nb, Mo, and C) were identified at grain boundaries by EDS analysis of the built plane, see the white precipitates in Fig. 5. Carbides in SLM-In718 provide second-phase strengthening which is best achieved at an elevated temperatures of 1080°C during the ST procedure [63]. Precipitation temperature of NbC was evaluated to be 1080°C using thermodynamical calculations [64] and for quenching, it was reported to be in

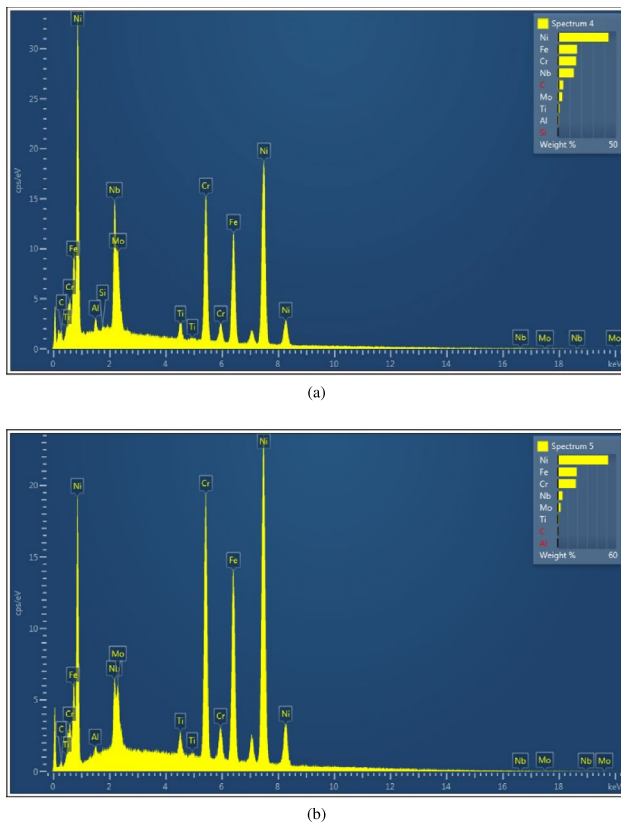


Fig. 3 Identification of phases in AB condition through EDS spectrum, intensity of elements versus energy (keV) for **a** Laves phase and **b** γ matrix

the range of 1243 – –1293°C provided that a certain cooling rate is used [34]. Obviously, the current ST procedure at 980°C could not completely develop carbide phases, but rather composite particles made of Laves and δ phases [63]. Abundance of second-phase carbide particles could help grain boundary pinning and resist against dislocation slips, which improve the hardening step during plastic deformation and thus the strength. Nevertheless, over-development of carbide particles could result in continuous brittle carbide films on the grain boundaries during ageing which are potential crack initiation points [65]. No carbide films were identified in the micrograph. Therefore, a temperature range of 1080 – –1160°C [64] seems to be enough for developing carbide particles and avoiding film formation during ST.

3.3 Compressive mechanical properties of TPMS structures

Surface quality and defects in fabricated TPMS structures

In the fabricated TPMS structures, internal pores cause discrepancies (between the nominal/designed and actual/fabricated properties) whereas powder particles additionally

affect the surface quality. Generally, TPMS parts created by SLM suffer from the following major defects:

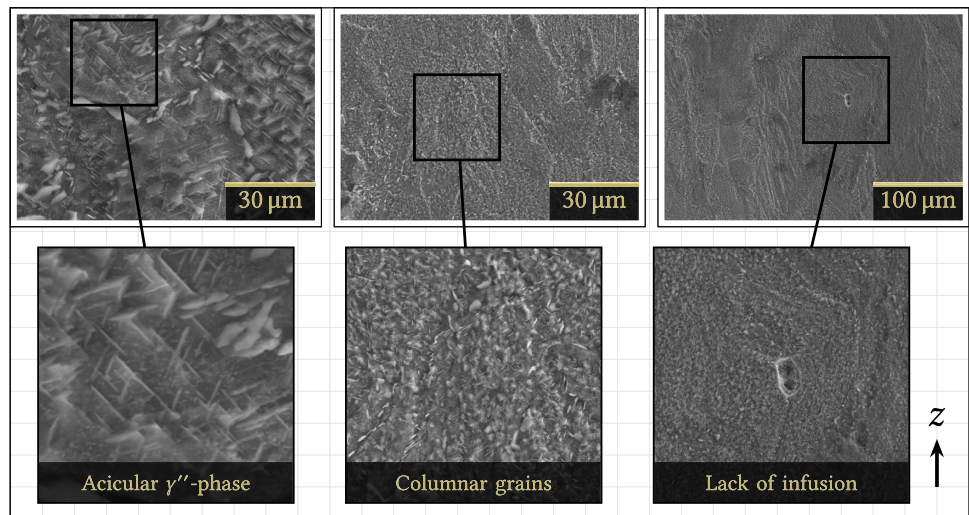
1. *Powder particles*; owing to the complex geometry of TPMS structures, removing the powder particles from internal surfaces is extremely challenging. As a consequence, these particles give rise to discrepancies between the designed and manufactured TPMS parts, e.g., higher surface roughness, susceptibility to crack initiation, and extra mass in the manufactured specimens [26]. Trapped particles originate from the powder bed during the molten state [66], see Fig. 6. Notably, the actual relative density was higher than the nominal relative density, see Table 2. For instance, the density of primitive specimens was measured to be 16.34% more than the designed value whereas gyroid specimens experienced the lowest increase of 10.03%.
2. *Internal pores*; the pores in the AB state are attributed to the gases emerging from the molten metal during the rapid solidification of SLM process [67]. Stress concentration forms around such pores and defects, deteriorating the mechanical response.

Optimising the SLM parameters can minimise the porosity level and improve the surface quality which can minimise the discrepancies in relative density and improve the microstructure to some extent.

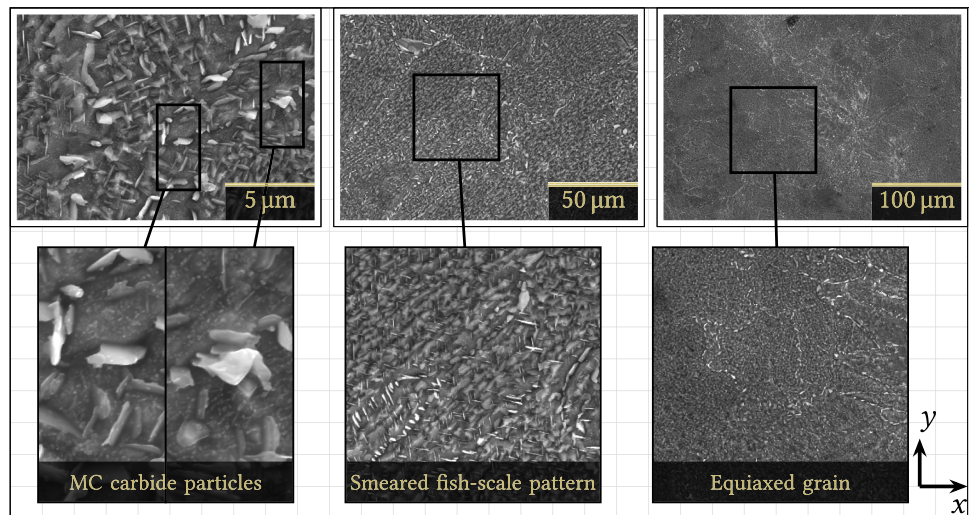
Stress–strain behaviour of TPMS structures Irrespective of the fluctuations at the plateau stage, the amount of absorbed energy improved for all TPMS specimens after heat treatment, see Fig. 7.¹ Mechanical response and performance is dictated by the deformation mechanism, which is a function of external stimuli, geometry, and material [15, 68]. Typical mechanical response of porous structures include linear elastic, plateau, and densification stages of which the elastoplastic plateau stage plays a key role in energy dissipation [55]. In the plateau stage, the behaviour of all AB TPMS specimens was quite stable whereas among the heat-treated samples, only the primitive specimen demonstrated a stable response, see Fig. 7c. Diamond and gyroid specimens showed a sudden loss of strength during plateau; a similar behaviour has been reported for a porous In718 specimen in [40]. Such fluctuations may appear more than once and has been reported for sheet-based TPMS structures made from other alloys too, e.g., AlSi10Mg [19]. In the same study, the fluctuations were alleviated after heat treatment. Plastic hinge formation cause internal structural instabilities that

¹ It should be noted that the experimental procedure was interrupted (around 42% strain) while testing diamond specimens because of reaching the load limit of the apparatus.

Fig. 4 SEM characterisation of In718 microstructure after SA treatment along build direction and on the build plane: **a** needle-shaped and columnar features of the γ matrix plus a defect on the grain boundary along the build direction (z -axis), and **b** carbide particles, removal of fish-scale pattern, and equiaxed grains on the build plane (xy -plane)



(a)



(b)

seem to be responsible for these occasional drops [69]. It should be noted that stretch-dominated behaviour usually experiences such fluctuations after the initial yield [70]. Nevertheless, manufacturing imperfections and misalignments during compression tests can also affect localised plastic deformations [24, 71]. In this sense, primitive specimens have demonstrated the most stable response, which was also confirmed by their symmetrical deformed configuration, see Fig. 7c.

Macroscopic deformation modes of TPMS specimens Macroscopic deformation modes of TPMS samples, as a function of topology, were affected by heat treatment, see Fig. 7. The localised failure modes can be related to the stress–strain response [69]:

- Diamond TPMS structures showed a unilateral shear band and an overall tilting of the structure (similar to simple shear deformation), see Fig. 7a. In the AB condition, uniform compression of the sample accompanied the shear band formation, which was presented as a gradually increasing plateau stage. In contrast, more localised compression and internal collapse were observed in the vicinity of the compressing plate at HT condition. Unilateral and bilateral shear band formation were reported in the literature for compression testing [9]. The softening behaviour in the stress–strain correspond to such instabilities during the experiments.
- Gyroid specimens showed a gradual and rather uniform compression (except closer to the compressive plate) in the AB condition whereas a unilateral shear band was formed in the HT sample, see Fig. 7b. This diagonal failure has presented itself as a sudden loss of stiffness in

Fig. 5 EDS analysis of the white carbide phase in SA In718

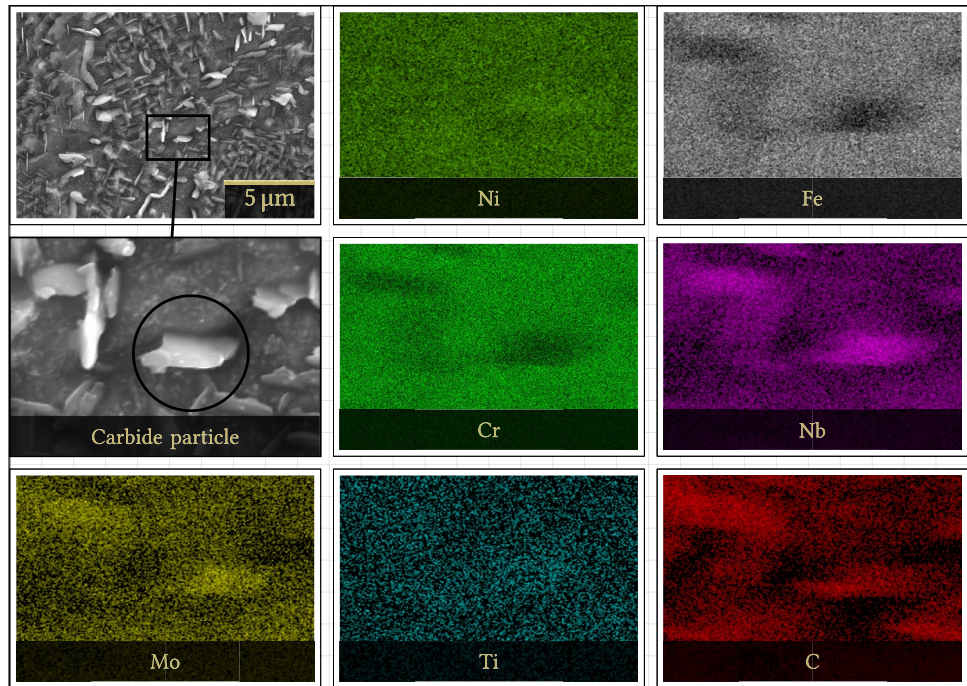


Fig. 6 Surface quality of diamond, gyroid, and primitive TPMS structures including the unsolidified particles

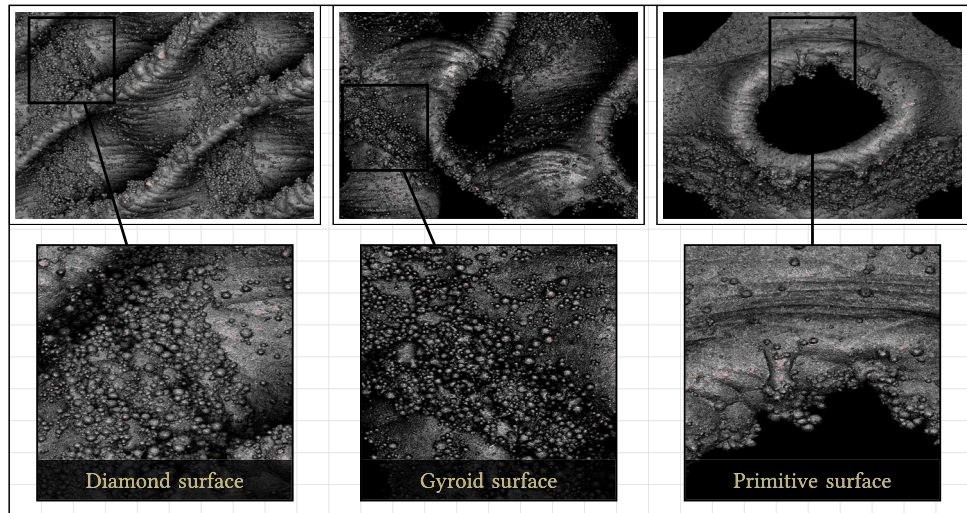
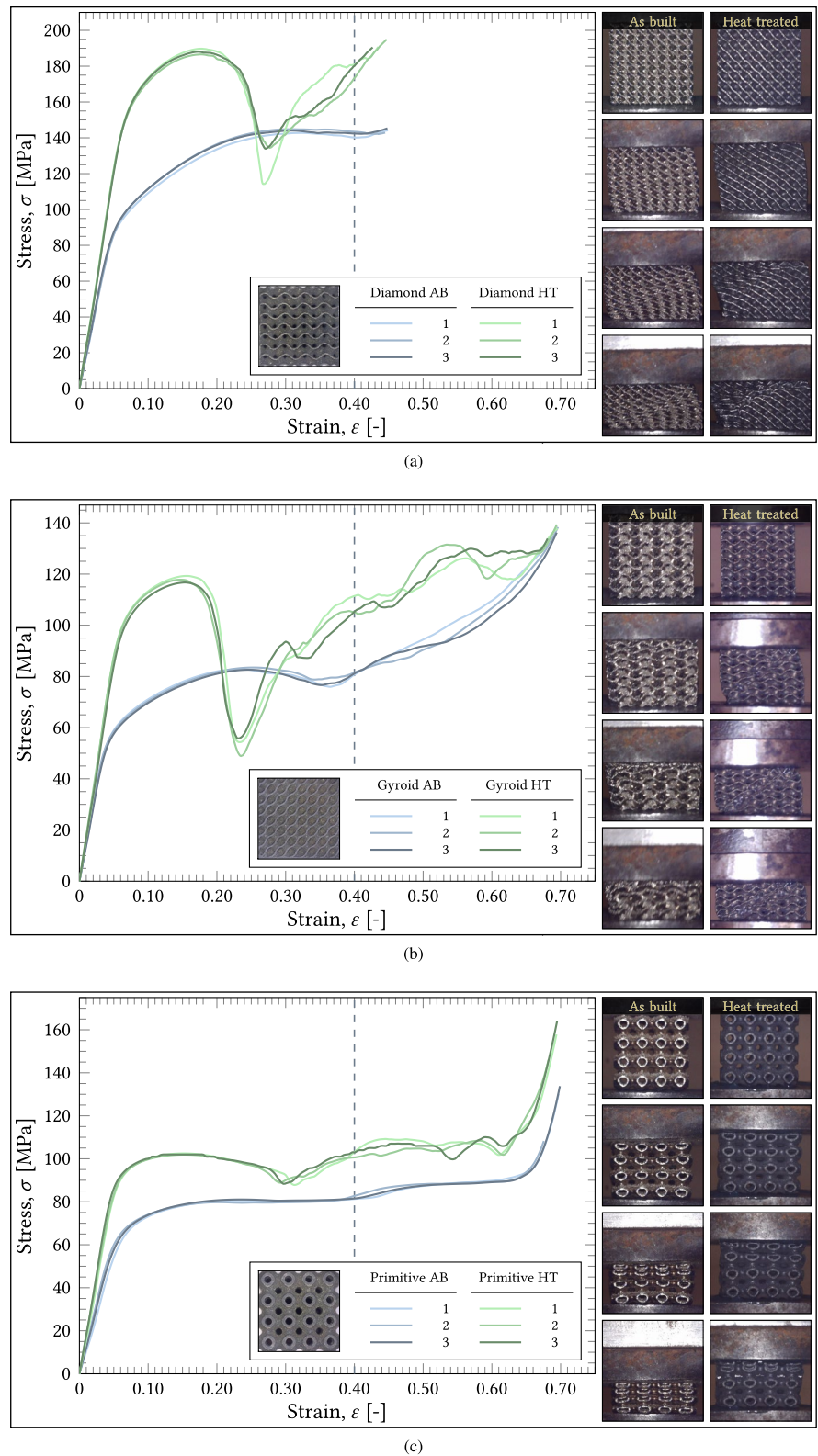


Table 2 Measured and calculated, average mass and density of the SLM TPMS structures

Geometry	Mass		Density		Relative density	
	Calculated \tilde{m} (g)	Measured m (g)	Calculated $\tilde{\rho}$ (g/cm ³)	Measured ρ (g/cm ³)	Calculated $\tilde{\rho}_r$ (-)	Measured ρ_r (-)
Diamond	8.051	9.007 [11.87%] [†]	1.966	2.199 [11.87%]	0.240	0.268 [11.87%]
Gyroid	6.370	7.009 [10.03%]	1.555	1.711 [10.03%]	0.190	0.209 [10.03%]
Primitive	7.710	8.970 [16.34%]	1.882	2.190 [16.34%]	0.230	0.267 [16.34%]

[†]Numbers in brackets denote the percentage increase in mass and density of fabricated TPMS compared to design values

Fig. 7 Stress–strain response of TPMS specimens in the AB and HT conditions for **a** diamond, **b** gyroid, and **c** primitive specimens. On the right-hand side of each graph, the progression of deformation in AB and HT samples is depicted



the stress–strain graph, see Fig. 7b. Similar shear band formation has been reported for this structure in the literature [9]. Shallow drops during the softening behaviour in the stress–strain are because of more localised insta-

bilities, similar to the modes during inclined loading of auxetics [17].

- Primitive TPMS structures were compressed almost perfectly without misalignment. In the AB state, a rather

uniform compression was observed whereas a layer-by-layer compression was obtained in the HT condition, see Fig. 7c. Collapse of each layer in the HT condition was reflected as slight drops in the stress–strain response. Diagonal shear band formation is also possible in primitive structures [9], which was not observed in this study.

Strain softening was observed in HT diamond and HT gyroid specimens while their AB behaviour lacked such severe fluctuations. Primitive specimen in both AB and HT conditions demonstrated the most stable deformation mechanism.

Mechanical properties of TPMS structures after SA After SA, elastic modulus, specific energy absorption, and end of plateau stress were improved while most of ductility measures deteriorated, see Table 3. Apparent elastic modulus (E) of the primitive sample was improved by 45.67% while gyroid specimens experienced a modest 19.01% increase. End of plateau stress (σ_{ple}) followed a similar pattern but with highest and lowest improvements amounting to 19.52% and 4.4% for primitive and gyroid samples, respectively. After SA, precipitation of γ' and γ'' second phases in the matrix along with δ -phase and carbides at the grain boundary impedes the cross-grain motion of dislocations during plastic flow and provides additional strength to material; similar observations were reported in [60, 63, 72]. An additional advantage of heat treatment is relieving the residual stresses which also works in favour of strength. Nevertheless, the strength–ductility trade-off will be present.

Ductility after SA Typical metrics for ductility are final strain, percentage relative deformation, and percentage reduction in cross-sectional area [73]. In the context of

porous materials, yield strain (ϵ_y), end of plateau strain (ϵ_{ple}), and strain corresponding to first local maximum stress (ϵ_{max}) can be used. Ductility of TPMS specimens appeared to be governed by unit cell topology and microstructure of the base material. For instance, gyroid samples experienced a 50.54% improvement in yield strain while primitive structure remained almost the same (only 0.66% improvement) after heat treatment. Along the same argument, first local peak in gyroid samples appeared earlier (a 37.49% reduction in strain) while primitive specimens showed a delayed peak after heat treatment (a 14.29% increase in strain). End of plateau strain decreased for gyroid and primitive samples which indicates a shrinkage in the plateau step. Effect of topology in reacting to an identical heat treatment is evident. Overall, it seems that an increase in strength values accompanies the loss of ductility. Consequently, very similar specific energy absorption (W_s) values were obtained for the specimens, all varying in the range of 22.42–27.45% after heat treatment. Yield enhancement and the delay in first yield stress are consequences of relieving the residual stresses and thus, postponing the initiation of plasticity at locations of stress concentration. Effect of topology seems to be prominent in this context, which could be investigated further by computational approaches such as finite element method [74–77]. Note that for the sake of comparison, toughness and energy absorption values were calculated up to 40% stain, unless stated otherwise.

Energy absorption efficiency in the AB and SA conditions Energy absorption efficiency has slightly improved after SA especially in the mid-range strain values (20–40% strain), see Fig. 8a. All graphs follow this pattern: a quadratic increase in the linear elastic region, almost a linear increase

Table 3 Compressive properties of three TPMS structures

Property	Condition	Diamond	Gyroid	Primitive
E [MPa]	AB	1917.69 ± 65.63	1744.22 ± 27.65	1218.79 ± 62.00
	HT	2371.78 ± 7.88 (23.68%) [†]	1465.65 ± 32.41 (19.01%)	1775.42 ± 56.79 (45.67%)
σ_{ple} [MPa]	AB	184.52 ± 1.71	104.78 ± 0.91	104.59 ± 0.52
	HT	208.01 ± 2.97 (12.73%)	109.39 ± 1.23 (4.4%)	124.90 ± 0.66 (19.42%)
ϵ_{ple} [%] [‡]	AB	44.47 ± 0.41	58.81 ± 0.68	67.37 ± 0.24
	HT	43.60 ± 1.03 (9.75%)	44.29 ± 1.60 (−24.69%)	66.42 ± 0.37 (−1.41%)
ϵ_y [%]	AB	4.36 ± 0.16	3.62 ± 0.04	4.79 ± 0.32
	HT	6.38 ± 0.02 (46.51%)	5.45 ± 0.03 (50.54%)	4.82 ± 0.14 (0.66%)
ϵ_{max} [%]	AB	30.05 ± 0.77	24.35 ± 0.45	22.31 ± 1.60
	HT	17.58 ± 0.25 (−41.50%)	15.22 ± 0.39 (−37.49%)	25.50 ± 15.91 (14.29%)
W_s [$\frac{\text{MJ}}{\text{kg}\cdot\text{m}^3}$]	AB	5.32 ± 0.05	8.25 ± 0.08	6.12 ± 0.14
	HT	6.79 ± 6.77 (27.54%)	10.10 ± 0.13 (22.42%)	7.61 ± 0.14 (24.23%)

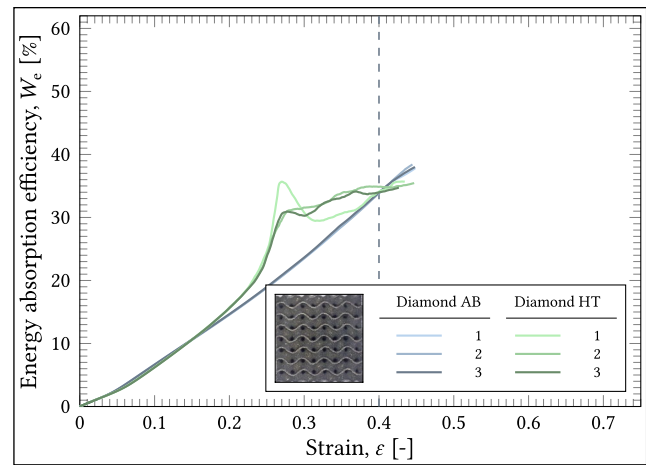
[†]Numbers in parentheses denote the percentage change of a property after heat treatment compared to the AB condition

[‡]End of plateau for diamond samples were taken as the final strain because of premature interruption of their experiments

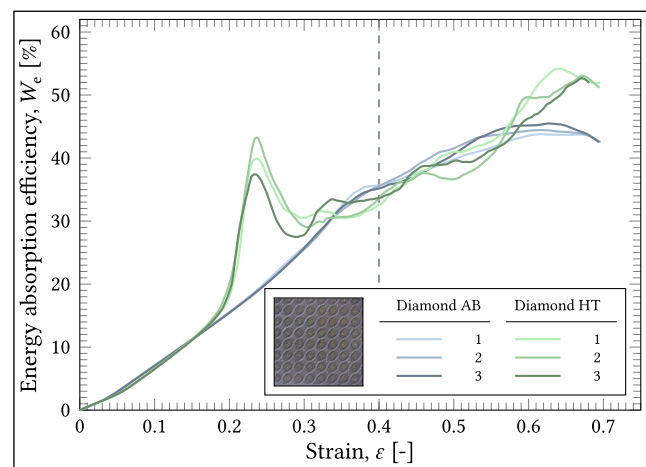
at the plateau stage, and a stationary point at the end of plateau. All samples after SA showed a jump around 30% strain which corresponds to the softening part of the stress–strain curve. Namely, energy efficiency is improved when higher strain energy is absorbed at a low stress level. Consequently, the maximum stationary point of the efficiency curve marks the beginning of densification (end of plateau) [69]. For instance, primitive structure shows a distinctive maximum point (Fig. 8c) whereas a more gradual local maximum is observed in gyroid specimens (Fig. 8c). These points correspond to the abrupt densification of primitive structures and a more gradual stress rise in gyroid samples, respectively (see Figs. 7b, c). Final point is that the stability of stress–strain behaviour is also reflected in the efficiency graph, e.g., the primitive structure showed very mild fluctuations in efficiency. Overall, the energy efficiency defined by Eq. (6) could not really report any distinctions between the response of the specimens. Additionally, since the relative density of the specimens was not the same (Table 2), comparing absolute values does not provide adequate insight. In the following section, a more detailed analysis of the normalised values is provided.

3.4 Normalised parameters and energy absorption of TPMS structures

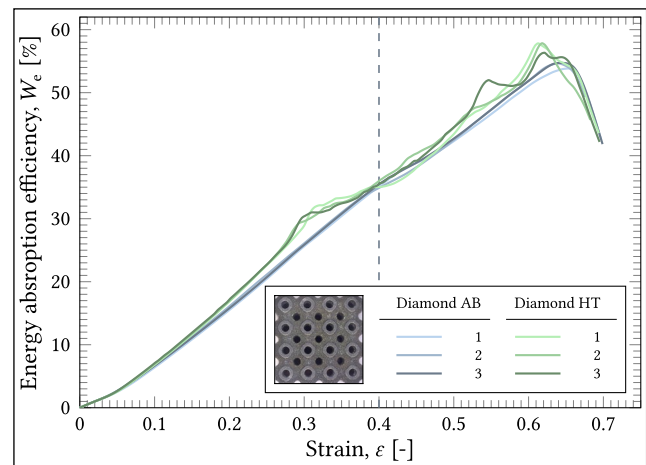
Normalised strength parameters After SA, normalised yield strength ($\bar{\sigma}_y$), normalised plateau strength ($\bar{\sigma}_{pl}$), and normalised first local maximum strength ($\bar{\sigma}_{max}$) were improved, see Fig. 9a. Diamond specimen showed the highest normalised strength parameters while primitive structure demonstrated the smallest performance. After heat treatment, the yield strength of the diamond structure improved by 84.13% followed by gyroid and primitive structures, i.e., 82.27% and 48.07%, respectively. This considerable increase is attributed to the activated strengthening mechanisms mentioned earlier, e.g., second phase precipitation, grain refinement and boundary pinning. Similarly, the first local peak of gyroid, diamond, and primitive structures experience an increase of 30.94%, 42.09%, 29.00%, respectively. Plateau stress of primitive, diamond, and gyroid samples increased by 19.42%, 12.73%, and 4.40%, respectively. It seems that strength parameters are governed more by topology than heat treatment. In other words, the extent of improvement in normalised strength parameters depends on the topology of TPMS structure.



(a)



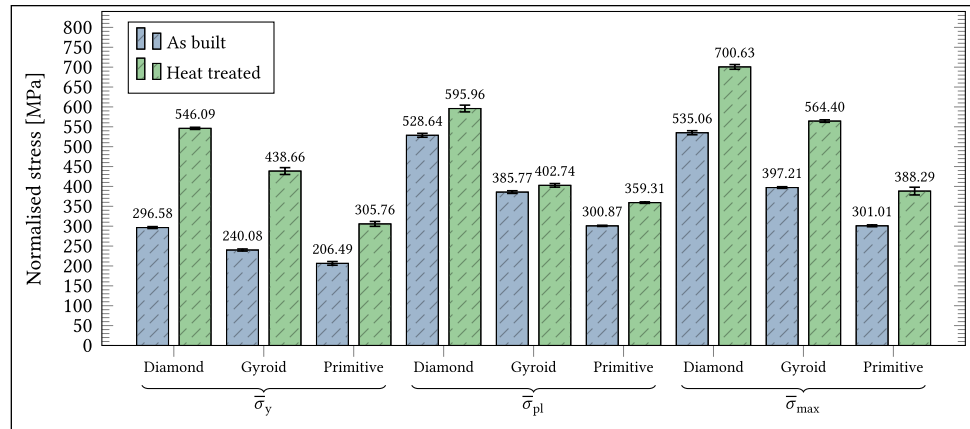
(b)



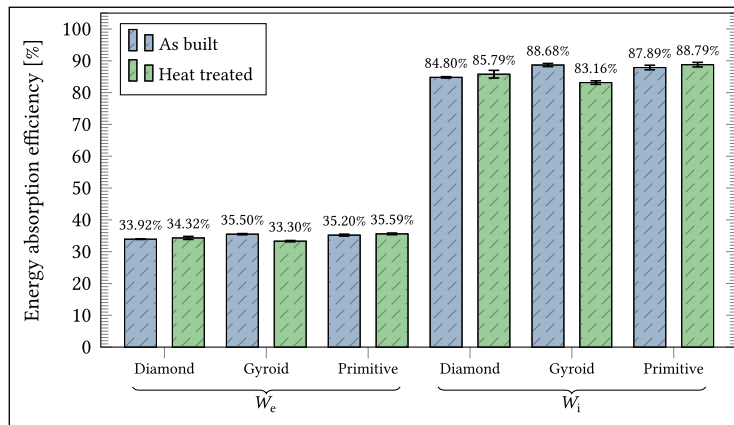
(c)

Fig. 8 Energy efficiency of TPMS specimens in the AB and HT conditions for **a** diamond, **b** gyroid, and **c** primitive specimens

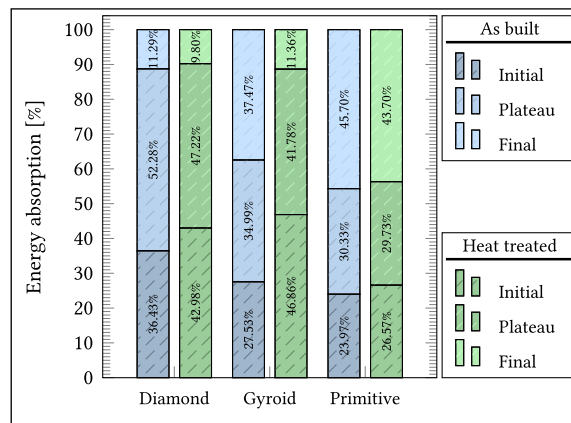
Fig. 9 Performance of TPMS structures in AB and HT conditions: **a** various strength metrics normalised with respect to relative density, **b** energy absorption efficiency (W_e) and ideality values (W_i) at $\epsilon = 0.4$, and **c** contribution of initial, plateau, and final stages of deformation to total energy absorption



(a)



(b)



(c)

Energy absorption efficiency and ideality The energy absorption efficiency of specimens and ideality percentage demonstrated similar relations but at different levels, see Fig. 9b. Up to 40%, energy efficiency of TPMS structures ranged between 33.30 and 35.59% in the AB and HT conditions. Similarly, ideality percentages were about

83.16–88.89% and thus, none of these metrics showed an extreme improvement in energy dissipation. Counter-intuitively, gyroid samples experienced a slight decrease according to both metrics. A single point on the efficiency graph does not provide a comprehensive picture on the structural

response. Therefore, investigating the strain energy fractions at various deformation stages seems to be an interesting idea.

Stage-wise strain energy absorption Conventionally, porous materials undergo three deformation stages: linear, plateau, and densification [24, 71]. Linear stage is quite short and elastic while densification is often excluded in the analysis because the important contributor to toughness is the plateau stage. Standard plateau stress is the arithmetic average of stresses in the range of 20–40% and end of plateau is officially denoted by 1.3 times thereof [53]. Based on these assumptions, the strain energy behaviour of TPMS specimens could be analysed in the following three stages:

- I. *initial stage* covers the traditional elastic region and a portion of plateau stress up to 20% strain;
- II. *plateau stage* encompasses the majority of conventional plateau in the range of 20–40% strain; and
- III. *final stage* is the remaining part of traditional plateau up to the upper limit point (i.e., beginning of densification).

According to the proposed classification, each TPMS specimen leaves a specific signature in terms of strain absorption, i.e., for the same energy absorption efficiency, the contribution at each stage varies based on the structure, see Fig. 9c. Dissipation of energy in the initial and plateau stages were increased after heat treatment while the final stage contracted. This behaviour summarises the consequences of SA into a single picture:

- increasing yield stress/strain and first local peak stress (along with decreasing its corresponding strain) contributes to the increase in the initial stage;
- increasing the plateau stress adds to the contribution of the plateau stage;
- and increasing the end of plateau stress and reduction of its respective strain results in a decrease of energy absorption at the final stage.

The overall trend is that energy absorption is pushed towards the initial and middle stages of deformation after heat treatment while the final stage is shrunk. This effect is closely related to the aforementioned strengthening mechanisms which work more in favour of strength than ductility.

4 Concluding remarks

Summary of the key findings In this study, it was hypothesised that heat treatment of TPMS structures can improve their mechanical properties. More specifically, it was aimed

to investigate the effect of standard heat-treatment on the microstructural evolution of bulk In718 samples and the mechanical properties of three TPMS In718 structures (diamond, gyroid, and primitive). It was found that overall performance of the HT structures has been improved in terms of key material parameters, leading to a change in the energy absorption signature compared to the AB state. In this sense, the following points can be highlighted:

- Among the investigated TPMS structures, diamond possesses the best values of all the mechanical properties followed by gyroid and primitive. The deformation modes and stress–strain behaviour were distinct for each TPMS structure. The mechanical properties of TPMS are governed by unit cell topology and internal microstructure. However, their impact on the mechanical properties is not equal.
- Heat treatment has altered the deformation modes of the tested TPMS structures from bending-dominated to stretch-dominated—where the latter is preferred because of its improved stiffness and strength.
- AB In718 TPMSs possesses non-equilibrium microstructure and detrimental phases. SA treatment resulted in the precipitation of γ' and γ'' -strengthening phases in matrix, δ -phase at grain boundaries, and the dissolution of some brittle Laves phases.
- SA greatly improved the mechanical properties of TPMS structures and resulted in a more stable mechanical response, owing to microstructure alteration. The highest increase was observed in terms of yield strength, followed by compressive strength, and Young's modulus. Plateau stress was least impacted by heat treatment.

For a specific heat treatment procedure, topology plays a critical role in obtaining an optimised response and maximising the specific properties. Therefore, the performance of SLM TPMS structures can be controlled by selecting an appropriate heat treatment process for the right topology.

Conclusion Although the recommended heat treatment procedure seems to improve the EA of the structures, the extent of enhancement was dictated by the topology of the TPMS structure. Microstructural transformations could justify most of the changes in the mechanical response. Overall, an improvement in strength was accompanied by a reduction in ductility. Thus, an analysis scheme was suggested to characterise the redistribution of energy absorption. Energy absorption was analysed in the classified initial, plateau, and final stages which encompass both strength and ductility variations after heat treatment. It was found that SA contributes mostly to the mechanical parameters that enhances energy absorption in the first two stages while slightly diminishing the contribution of the final stage. SLM In-718 could take

advantage of the conventional SA mostly in improving the strength parameters and some of the ductility metrics. In terms of energy absorption, the overall efficiency remains rather unchanged after SA but more dissipation is shifted towards the first two stages of deformation.

Future work To further challenge the capabilities of TPMS structures, quantifying the manufacturing imperfections would shed light on the controlling factors of deformation/failure mechanisms. This issue becomes more pronounced when geometrical features are printed in scales closer to the resolution of the apparatus. Another focus could be enhancing the heat treatment procedure and/or geometry design to improve the material performance in providing a more stable plateau response for controlled energy absorption. Finally, the relation between localised plasticity at stress concentration locations and the new energy analysis scheme can be studied using computational approaches.

Acknowledgements The authors would like to thank the Advanced Design and Prototyping Technologies (ADaPT) Institute at Griffith University for providing the samples and conducting the heat treatment procedures. In addition, the authors would like to thank Professor Stefanie Feih for her support during this study.

Funding Open Access funding enabled and organized by CAUL and its Member Institutions.

Data availability Experimental data is available upon reasonable request.

Declarations

Conflict of interest The authors declare that there is no Conflict of interest or Conflict of interest for the research work.

Open Access This article is licensed under a Creative Commons Attribution 4.0 International License, which permits use, sharing, adaptation, distribution and reproduction in any medium or format, as long as you give appropriate credit to the original author(s) and the source, provide a link to the Creative Commons licence, and indicate if changes were made. The images or other third party material in this article are included in the article's Creative Commons licence, unless indicated otherwise in a credit line to the material. If material is not included in the article's Creative Commons licence and your intended use is not permitted by statutory regulation or exceeds the permitted use, you will need to obtain permission directly from the copyright holder. To view a copy of this licence, visit <http://creativecommons.org/licenses/by/4.0/>.

References

- Al-Ketan O, Lee D-W, Rowshan R, Abu Al-Rub RK (2020) Functionally graded and multi-morphology sheet TPMS lattices: design, manufacturing, and mechanical properties. *J Mech Behav Biomed Mater* 102:103520. <https://doi.org/10.1016/j.jmbbm.2019.103520>
- Han L, Che S (2018) An overview of materials with triply periodic minimal surfaces and related geometry: from biological structures to self-assembled systems. *Adv Mater* 30(17):1705708. <https://doi.org/10.1002/adma.201705708>
- Alabort E, Barba D, Reed RC (2019) Design of metallic bone by additive manufacturing. *Scr Mater* 164:110–114. <https://doi.org/10.1016/j.scriptamat.2019.01.022>
- Majeed M, Khan HM, Wheatley G, Situ R (2022) Influence of post-processing on additively manufactured lattice structures. *J Braz Soc Mech Sci Eng* 44(9):1–28. <https://doi.org/10.1007/s40430-022-03703-8>
- Ebrahimzadeh Dehaghani A, Javanbakht Z, Barzan M, Lloyd DG, Feih S (2024) Multifunctional design of triply periodic minimal surface structures for temporary pediatric fixation devices. *Adv Eng Mater*. <https://doi.org/10.1002/adem.202400518>
- Javanbakht Z, Hall W, Öchsner A (2018) Improved performance of materials computational evaluation of transverse thermal conductivity of natural fiber composites Springer international publishing cham 197-206
- Bobbert FSL, Lietaert K, Eftekhari AA, Pouran B, Ahmadi SM, Weinans H, Zadpoor AA (2017) Additively manufactured metallic porous biomaterials based on minimal surfaces: a unique combination of topological, mechanical, and mass transport properties. *Acta Biomater* 53:572–584. <https://doi.org/10.1016/j.actbio.2017.02.024>
- Al-Ketan O, Adel Assad M, Abu Al-Rub RK (2017) Mechanical properties of periodic interpenetrating phase composites with novel architected microstructures. *Compos Struct* 176(9–19):0263–8223. <https://doi.org/10.1016/j.compstruct.2017.05.026>
- Al-Ketan O, Rowshan R, Abu Al-Rub RK (2018) Topology-mechanical property relationship of 3D printed strut, skeletal, and sheet based periodic metallic cellular materials. *Addit Manuf* 19:167–183. <https://doi.org/10.1016/j.addma.2017.12.006>
- Qiu N, Wan Y, Shen Y, Fang J (2024) Experimental and numerical studies on mechanical properties of TPMS structures. *Int J Mech Sci* 261:108657. <https://doi.org/10.1016/j.ijmecsci.2023.108657>
- Kadkhodapour J, Montazerian H, Raeisi S (2014) Investigating internal architecture effect in plastic deformation and failure for TPMS-based scaffolds using simulation methods and experimental procedure. *Mater Sci Eng C Mater Biol Appl* 43:587–597. <https://doi.org/10.1016/j.msec.2014.07.047>
- Khaderi SN, Deshpande VS, Fleck NA (2014) The stiffness and strength of the gyroid lattice. *Int J Solids Struct* 51(23–24):3866–3877. <https://doi.org/10.1016/j.ijsolstr.2014.06.024>
- Choy SY, Sun C-N, Leong KF, Wei J (2017) Compressive properties of Ti–6Al–4V lattice structures fabricated by selective laser melting: design, orientation and density. *Addit Manuf* 16:213–224. <https://doi.org/10.1016/j.addma.2017.06.012>
- Deshpande VS, Ashby MF, Fleck NA (2001) Foam topology: bending versus stretching dominated architectures. *Acta Mater* 49(6):1035–1040. [https://doi.org/10.1016/S1359-6454\(00\)00379-7](https://doi.org/10.1016/S1359-6454(00)00379-7)
- Hassani F, Javanbakht Z (2020) Adjusting the plastic zone development in steel plate shear walls—a finite element study. In: Öchsner A, Altenbach H (eds) *Engineering design applications III*. Advanced structured materials, vol 124. Springer International Publishing, Cham, pp 337–348. https://doi.org/10.1007/978-3-030-39062-4_27
- Javanbakht Z, Abmus M, Naumenko K, Öchsner A, Altenbach H (2019) On thermal strains and residual stresses in the linear theory of anti-sandwiches. *Zeitschrift für Angewandte Mathematik und Mechanik*. <https://doi.org/10.1002/ZAMM.201900062>
- Dhari RS, Hall W, Asthana A, Javanbakht Z (2023) Direct FE2 analysis of additively manufactured parts with voids. *Mater Today Proc*. <https://doi.org/10.1016/j.matpr.2023.05.124>
- Jam A, Pellizzari M, Emanuelli L, Valsecchi G, Du Plessis A, Benedetti M (2023) Influence of heat treatment on the mechanical performance of Ti21S octet truss lattice structure fabricated

- by laser powder bed fusion. *Prog Addit Manuf*. <https://doi.org/10.1007/s40964-023-00494-9>
19. Sun Q, Sun J, Guo K, Liu J (2022) Investigation on mechanical properties and energy absorption capabilities of AlSi10Mg triply periodic minimal surface sheet structures fabricated via selective laser melting. *J Mater Eng Perform* 31(11):9110–9121. <https://doi.org/10.1007/s11665-022-06883-5>
 20. Nie Y, Tang Q, Zhao M, Song J (2023) Effect of heat treatment on mechanical properties, failure modes and energy absorption characteristics of lattice skeleton and sheet structures fabricated by SLM. *J Mark Res* 26:4925–4941. <https://doi.org/10.1016/j.jmrt.2023.08.264>
 21. F42 Committee: Specification for additive manufacturing nickel alloy (UNS N07718) with powder bed fusion. ASTM International, West Conshohocken, PA. <https://doi.org/10.1520/F3055-14A>
 22. Schneider J, Lund B, Fullen M (2018) Effect of heat treatment variations on the mechanical properties of Inconel 718 selective laser melted specimens. *Addit Manuf* 21:248–254. <https://doi.org/10.1016/j.addma.2018.03.005>
 23. Karimi M, Khoshgoftar MJ, Karimi M, Mirzaali MJ, Javanbakht Z (2023) An analytical model for the static behaviour of honeycomb sandwich plates with auxetic cores using higher-order shear deformation theories. *Int J Mech Mater Des* 19(4):951–969. <https://doi.org/10.1007/s10999-023-09667-4>
 24. Hassani F, Javanbakht Z, Malek S (2024) Large deformation behavior and energy absorption of rotating square auxetics. *Compos B Eng*. <https://doi.org/10.1016/j.compositesb.2024.111596>
 25. Deshpande VS, Fleck NA, Ashby MF (2001) Effective properties of the octet-truss lattice material. *J Mech Phys Solids* 49(8):1747–1769
 26. Yang L, Mertens R, Ferrucci M, Yan C, Shi Y, Yang S (2019) Continuous graded gyroid cellular structures fabricated by selective laser melting: design, manufacturing and mechanical properties. *Mater Des* 162:394–404. <https://doi.org/10.1016/j.matdes.2018.12.007>
 27. Du Plessis A, Razavi N, Benedetti M, Murchio S, Leary M, Watson M, Bhate D, Berto F (2022) Properties and applications of additively manufactured metallic cellular materials: a review. *Prog Mater Sci* 125:100918. <https://doi.org/10.1016/j.pmatsci.2021.100918>
 28. Heilgeist S, Heine B, Merkel M, Hitzler L, Javanbakht Z, Öchsner A (2019) The influence of post-heat treatments on the tensile strength and surface hardness of selectively laser-melted AlSi10Mg. *Materialwissenschaft und Werkstofftechnik* 50(5):546–552. <https://doi.org/10.1002/MAWE.201800236>
 29. Alhammadi A, Al-Ketan O, Khan KA, Ali M, Rowshan R, Abu Al-Rub RK (2020) Microstructural characterization and thermo-mechanical behavior of additively manufactured AlSi10Mg sheet cellular materials. *Mater Sci Eng A* 791:139714. <https://doi.org/10.1016/j.msea.2020.139714>
 30. Yan X, Yue S, Ge J, Chen C, Lupoi R, Yin S (2022) Microstructural and mechanical optimization of selective laser melted Ti6Al4V lattices: effect of hot isostatic pressing. *J Manuf Process* 77:151–162. <https://doi.org/10.1016/j.jmapro.2022.02.024>
 31. Xiang DD, Wang P, Tan XP, Chandra S, Wang C, Nai MLS, Tor SB, Liu WQ, Liu E (2019) Anisotropic microstructure and mechanical properties of additively manufactured Co–Cr–Mo alloy using selective electron beam melting for orthopedic implants. *Mater Sci Eng A* 765:138270. <https://doi.org/10.1016/j.msea.2019.138270>
 32. Ravichander BB, Jagdale SH, Javed A, Kumar G (2023) Mechanical and corrosion behavior of sheet-based 316L TPMS structures. *Int J Mech Sci* 254:108439. <https://doi.org/10.1016/j.ijmecsci.2023.108439>
 33. Karmuhilan M, Kumanan S (2022) A review on additive manufacturing processes of Inconel 625. *J Mater Eng Perform* 31(4):2583–2592. <https://doi.org/10.1007/s11665-021-06427-3>
 34. Antonsson T, Fredriksson H (2005) The effect of cooling rate on the solidification of INCONEL 718. *Metall Mater Trans B* 36(1):85–96. <https://doi.org/10.1007/s11663-005-0009-0>
 35. Renishaw: In718-0405 powder for additive manufacturing. Data sheet, Renishaw plc
 36. Qi H, Azer M, Ritter A (2009) Studies of standard heat treatment effects on microstructure and mechanical properties of laser net shape manufactured INCONEL 718. *Metall Mater Trans A* 40(10):2410–2422. <https://doi.org/10.1007/s11661-009-9949-3>
 37. Alkebsi EAA, Ameddah H, Outtas T, Almutawakel A (2021) Design of graded lattice structures in turbine blades using topology optimization. *Int J Comput Integr Manuf* 34(4):370–384. <https://doi.org/10.1080/0951192X.2021.1872106>
 38. Xu L, Chai Z, Peng B, Zhou W, Chen X (2023) Effect of heat treatment on microstructures and mechanical properties of Inconel 718 additively manufactured using gradient laser power. *Mater Sci Eng A* 868:144754. <https://doi.org/10.1016/j.msea.2023.144754>
 39. Hosseini E, Popovich VA (2019) A review of mechanical properties of additively manufactured Inconel 718. *Addit Manuf* 30:100877. <https://doi.org/10.1016/j.addma.2019.100877>
 40. Zhao Z, Xu X, Wang Q, Bai P, Du W, Zhang L, Wang W (2021) Microstructure and properties of periodic porous Inconel 718 alloy prepared by selective laser melting. *Adv Compos Hybrid Mater* 4(2):332–338. <https://doi.org/10.1007/s42114-021-00240-1>
 41. Huang W, Yang J, Yang H, Jing G, Wang Z, Zeng X (2019) Heat treatment of Inconel 718 produced by selective laser melting: microstructure and mechanical properties. *Mater Sci Eng A* 750:98–107. <https://doi.org/10.1016/j.msea.2019.02.046>
 42. Ansari MJ, Nguyen D-S, Park HS (2019) Investigation of SLM process in terms of temperature distribution and melting pool size: modeling and experimental approaches. *Materials (Basel, Switzerland)*. <https://doi.org/10.3390/ma12081272>
 43. Naskar S, Rohila S, Suryakumar S, Panigrahi BB (2021) Influence of heat treatments on microstructure and mechanical properties of additively manufactured Inconel 718 superalloy. *Trans Indian Natl Acad Eng* 6(4):1049–1055. <https://doi.org/10.1007/s41403-021-00247-6>
 44. Popovich AA, Sufiarov VS, Polozov IA, Borisov EV (2015) Microstructure and mechanical properties of Inconel 718 produced by SLM and subsequent heat treatment. *Key Eng Mater* 651–653:665–670. <https://doi.org/10.4028/www.scientific.net/KEM.651-653.665>
 45. Fayed EM, Shahriari D, Saadati M, Brailovski V, Jahazi M, Medraj M (2020) Influence of homogenization and solution treatments time on the microstructure and hardness of Inconel 718 fabricated by laser powder bed fusion process. *Materials* 13(11):2574. <https://doi.org/10.3390/ma13112574>
 46. Babamiri BB, Indeck J, Demeneghi G, Cuadra J, Hazeli K (2020) Quantification of porosity and microstructure and their effect on quasi-static and dynamic behavior of additively manufactured Inconel 718. *Addit Manuf* 34:101380. <https://doi.org/10.1016/j.addma.2020.101380>
 47. Deng D, Peng RL, Brodin H, Moverare J (2018) Microstructure and mechanical properties of Inconel 718 produced by selective laser melting: sample orientation dependence and effects of post heat treatments. *Mater Sci Eng A* 713:294–306. <https://doi.org/10.1016/j.msea.2017.12.043>
 48. Li Z, Kuai Z, Li J, Liu B, Zhao M, Yang Z, Liu F, Bai P, Huo W (2023) Effect of heat treatment on compression properties of the 316L diamond structure fabricated through selective laser melting. *J Market Res* 25:5076–5095. <https://doi.org/10.1016/j.jmrt.2023.06.268>

49. Ge J, Huang Q, Wang Y, Zhang C, Liu Q, Lu Z, Yin S (2023) Microstructural optimization and mechanical enhancement of SLM Ti6Al4V TPMS scaffolds through vacuum annealing treatment. *J Alloys Compd* 934:167524. <https://doi.org/10.1016/j.jallcom.2022.167524>
50. AlMahri S, Santiago R, Lee D-W, Ramos H, Alabdouli H, Alteineji M, Guan Z, Cantwell W, Alves M (2021) The design of additively manufactured lattices to increase the functionality of medical implants. *Addit Manuf* 46:102220. <https://doi.org/10.1016/j.addma.2021.102220>
51. ASTM (2003) Standard specification for precipitation-hardening nickel alloy bars, forgings, and forging stock for high-temperature service. ASTM International
52. SAE International (1999) AMS 2773. Heat treatment cast nickel alloy and cobalt alloy parts
53. International Standard (2014) ISO 13314, Mechanical testing of metals—ductility testing ls—compression test for porous and cellular metals. ISO, Geneva
54. Tucho WM, Hansen V (2019) Characterization of SLM-fabricated Inconel 718 after solid solution and precipitation hardening heat treatments. *J Mater Sci* 54(1):823–839. <https://doi.org/10.1007/s10853-018-2851-x>
55. Dhari RS, Javanbakht Z, Hall W (2020) On the deformation mechanism of re-entrant honeycomb auxetics under inclined static loads. *Mater Lett*. <https://doi.org/10.1016/j.matlet.2020.129214>
56. Miltz J, Ramon O (1990) Energy absorption characteristics of polymeric foams used as cushioning materials. *Polym Eng Sci* 30(2):129–133. <https://doi.org/10.1002/pen.760300210>
57. Periane S, Duchosal A, Vaudreuil S, Chibane H, Morandea A, Anthony Xavier M, Leroy R (2021) Influence of heat treatment on the fatigue resistance of Inconel 718 fabricated by selective laser melting (SLM). *Mater Today Proc* 46:7860–7865. <https://doi.org/10.1016/j.matpr.2021.02.447>
58. Sui S, Tan H, Chen J, Zhong C, Li Z, Fan W, Gasser A, Huang W (2019) The influence of Laves phases on the room temperature tensile properties of Inconel 718 fabricated by powder feeding laser additive manufacturing. *Acta Mater* 164:413–427. <https://doi.org/10.1016/j.actamat.2018.10.032>
59. Tao P, Li H, Huang B, Hu Q, Gong S, Xu Q (2019) The crystal growth, intercellular spacing and microsegregation of selective laser melted Inconel 718 superalloy. *Vacuum* 159:382–390. <https://doi.org/10.1016/j.vacuum.2018.10.074>
60. Yang H, Wang Z, Wang H, Wu Y, Wang H (2023) Microstructure, mechanical property and heat treatment schedule of the Inconel 718 manufactured by low and high power laser powder bed fusion. *Mater Sci Eng A* 863:144517. <https://doi.org/10.1016/j.msea.2022.144517>
61. Zhang S, Lin X, Wang L, Yu X, Hu Y, Yang H, Lei L, Huang W (2021) Strengthening mechanisms in selective laser-melted Inconel718 superalloy. *Mater Sci Eng A* 812:141145. <https://doi.org/10.1016/j.msea.2021.141145>
62. Zhang HY, Zhang SH, Cheng M, Zhao Z (2017) Microstructure evolution of IN718 alloy during the delta process. *Procedia Eng* 207:1099–1104. <https://doi.org/10.1016/j.proeng.2017.10.1137>
63. Zhao Y, Guan K, Yang Z, Hu Z, Qian Z, Wang H, Ma Z (2020) The effect of subsequent heat treatment on the evolution behavior of second phase particles and mechanical properties of the Inconel 718 superalloy manufactured by selective laser melting. *Mater Sci Eng A* 794:139931. <https://doi.org/10.1016/j.msea.2020.139931>
64. Shu DL, Tian SG, Tian N, Xie J, Su Y (2017) Thermodynamic analysis of carbide precipitation and effect of its configuration on creep properties of FGH95 powder nickel-based superalloy. *Mater Sci Eng A* 700:152–161. <https://doi.org/10.1016/j.msea.2017.05.108>
65. Zhao X, Chen J, Lin X, Huang W (2008) Study on microstructure and mechanical properties of laser rapid forming Inconel 718. *Mater Sci Eng A* 478(1–2):119–124. <https://doi.org/10.1016/j.msea.2007.05.079>
66. DebRoy T, Wei HL, Zuback JS, Mukherjee T, Elmer JW, Milewski JO, Beese AM, Wilson-Heid A, De A, Zhang W (2018) Additive manufacturing of metallic components—process, structure and properties. *Prog Mater Sci* 92:112–224. <https://doi.org/10.1016/j.pmatsci.2017.10.001>
67. Monkova K, Monka PP, Pantazopoulos GA, Toulfatzis AI, Šmeringiová A, Török J, Papadopoulou S (2023) Effect of cross-head speed and volume ratio on compressive mechanical properties of mono- and double-gyroid structures made of Inconel 718. *Materials* 16(14):4973. <https://doi.org/10.3390/ma16144973>
68. Hassani F, Javanbakht Z (2020) Effect of geometrical variations on the failure mechanisms of perforated steel plate shear walls—a parametric study towards a new design. *Thin-Walled Struct*. <https://doi.org/10.1016/j.tws.2020.107244>
69. Dhari RS, Javanbakht Z, Hall W (2021) On the inclined static loading of honeycomb re-entrant auxetics. *Compos Struct* 273:114289. <https://doi.org/10.1016/j.compstruct.2021.114289>
70. Maconachie T, Leary M, Lozanovski B, Zhang X, Qian M, Faruque O, Brandt M (2019) SLM lattice structures: properties, performance, applications and challenges. *Mater Des* 183:108137. <https://doi.org/10.1016/j.matdes.2019.108137>
71. Hassani F, Javanbakht Z, Froese TM, Malek S (2023) Energy dissipative bio-inspired rotating square auxetics for building applications. In: Amiri L, Moreau S, Poncet S (eds) *Progress in Canadian mechanical engineering*, vol 6. Université de Sherbrooke. Faculté de génie, Sherbrooke. <https://doi.org/10.17118/111143/21158>
72. Wang W, Wang S, Zhang X, Chen F, Xu Y, Tian Y (2021) Process parameter optimization for selective laser melting of Inconel 718 superalloy and the effects of subsequent heat treatment on the microstructural evolution and mechanical properties. *J Manuf Process* 64:530–543. <https://doi.org/10.1016/j.jmapro.2021.02.004>
73. Callister WD Jr, Rethwisch DG (2020) *Fundamentals of materials science and engineering: an integrated approach*. Wiley, London
74. Javanbakht Z, Öchsner A (2017) *Advanced finite element simulation with MSC Marc: application of user subroutines*. Springer, Cham. <https://doi.org/10.1007/978-3-319-47668-1>
75. Javanbakht Z, Öchsner A (2018) *Computational statics revision course*. Springer International Publishing, Cham. <https://doi.org/10.1007/978-3-319-67462-9>
76. (2020) An element-wise scheme to analyse local mechanical anisotropy in fibre-reinforced composites. *Mat Sci Technol* 36(11):1178–1190. <https://doi.org/10.1080/02670836.2020.1762296>
77. Javanbakht Z, Hall W, Öchsner A (2017) The effect of substrate bonding on characterization of thin elastic layers: a finite element study abstract translation abstract. *Materialwissenschaft und Werkstofftechnik* 48(5):456–462. <https://doi.org/10.1002/mawe.201700035>

Publisher's Note Springer Nature remains neutral with regard to jurisdictional claims in published maps and institutional affiliations.